Contents lists available at ScienceDirect

Acta Materialia

Full length article

Effect of grain boundary character on intergranular hydrides precipitation in zirconium

Si-Mian Liu, Wei-Zhong Han [*]

Center for Advancing Materials Performance from the Nanoscale, State Key Laboratory for Mechanical Behavior of Materials, Xi'an Jiaotong University, Xi'an 710049, China

ABSTRACT

Grain boundary characteristics play a crucial role in the formation of intergranular hydrides, which may cause brittle fracture in zirconium alloys. However, the impact of grain boundary character on microscopic hydride precipitation remains unclear. Here, we investigate the nucleation and precipitation of intergranular hydrides in zirconium by using In-situ transmission electron microscopy observations and post-precipitation electron backscattered diffraction analysis. The nucleation of intergranular hydrides is highly dependent on the interacting angle (α_{GB-BP}) between the grain boundary plane and the basal plane. For low-angle grain boundaries, hydrides prefer to grow into the grain interior when the α_{GB-BP} is less than 60°, otherwise, no hydride precipitation occurs. For high-angle grain boundaries, hydrides nucleate along the grain boundary when the α_{GB-BP} is less than 39°. As the α_{GB-BP} increases, hydrides grow into the grain interior. A thermodynamic model is developed to analyze the nucleation of needle-shaped hydrides. The variation of the intergranular hydride as a function of the grain boundary energy and the α_{GB-BP} is predicted. This finding provides new insight into utilizing grain boundary engineering to modulate intergranular hydride precipitation and offers a pathway to control hydrogen embrittlement in zirconium alloys.

1. Introduction

Zirconium (Zr) alloys are widely used as fuel cladding tubes and pressure vessels in pressurized water nuclear reactors due to their attractive performance with a low thermal neutron capture cross-section, excellent corrosion resistance, high strength and creep resistance [1]. Zr alloys have a high affinity for hydrogen and readily uptake hydrogen in an acidic or hydrogen-rich environment [2]. Hydrogen has a very low solid solubility of less than 20 ppm at room temperature in Zr, and once the solid solubility of hydrogen is exceeded, brittle hydrides are widely precipitated in Zircaloy [2]. Due to the detrimental mechanical effects caused by the brittle hydrides on fuel cladding and pressure tubes, the precipitation behavior of Zr hydrides and their embrittlement effects have drawn broad research interest in the past decades [3–7].

Two types of hydrides are commonly observed in polycrystalline Zr alloys, intragranular hydrides and intergranular hydrides, which are classified based on their precipitation sites [8–16]. Individual intragranular hydrides show either needle shape or disc shape with a growth

direction parallel to $<11\bar{2}0>$ in the hexagonal close-packed (HCP) Zr lattice, and with the habit plane of (0001) under an equilibrium condition or reoriented to one of the pyramidal planes or prismatic planes under external tensile stress [5,9,10]. In contrast, the morphology of intergranular hydrides varies: (i) Some hydrides initiate at the grain boundary (GB), and grow into one or two adjacent grains; (ii) Some hydrides precipitate along the GB [11-14]. The majority of intergranular hydrides appear as plate-like or ellipsoidal shapes, have a size of several micrometers, and maintain a similar orientation relationship with the matrix as the intragranular hydrides [11–15]. However, intergranular hydrides are more deleterious to ductility than intragranular hydrides because they are the initiators of intergranular cracking [17].

Intergranular hydride precipitation is influenced by the characteristics of GBs. The dependence of intergranular hydrides on the crystallographic features of GBs has been assessed using a variety of parameters, including crystallographic orientation of the rotation axes and angles (axis-angle pair), interacting angle (α_{GB-BP}) between the GB and the basal plane (BP), c-axis misorientation, and coincident site lattice (CSL) notations [8–18]. Nonetheless, some contradictory findings

---

exist. Intergranular hydrides are thought to form preferentially on some specific GBs, such as GB planes parallel to the (0001) plane [12,17] or having an angle of 35–40° or 60–75° to the basal plane of adjacent grains [8]. In contrast, some results showed that intergranular hydrides precipitate on all types of GB in terms of the angle between GB and the basal plane [13]. Other researchers have found that intergranular hydrides are more likely to form on GBs with higher CSL values because they have higher GB energies, which favor hydride nucleation [17,18]. Nevertheless, some low-energy coherent GBs have been reported to be the preferred nucleation sites for intergranular hydrides, such as {$10\bar{1}2$} <$10\bar{1}1$> twin boundaries [19]. An additional parameter to characterize the properties of GBs is the c-axis misorientation. It has been reported that intergranular hydrides preferentially precipitate when the c-axis misorientation is less than 40° or greater than 80° [13]. Recent research revealed that GBs with c-axis misorientations between 55° and 60° are also preferred precipitation sites for subsurface intergranular hydrides [14]. As of yet, there is no agreement on the correlation between the characteristics of GBs and the preferential precipitation of intergranular hydride.

Electron backscattered diffraction (EBSD) can be used to determine the orientation relationship among intergranular hydrides, GBs, and matrix. However, the statistical results of intergranular hydrides may be somewhat limited because the observed mesoscopic hydrides are composed of multiple submicron hydrides [14,16,20]. After nucleation within or close to the GBs, individual hydride may expand or stack, thereby establishing a connection to the GBs [12]. If the nucleation of a single intergranular hydride can be captured, it is easier to get a clear relationship between GB character and intergranular hydrides. In-situ observation of hydride precipitation inside a transmission electron microscope (TEM) or using high-energy synchrotron X-ray diffraction are thought to be more efficient methods to identify the initiation site of hydride nucleation [21–23]. However, observing the nucleation of intergranular hydrides in real-time remains a challenge and has not yet been reported.

In this work, we employ in situ TEM to investigate the nucleation and precipitation of intergranular hydrides at room temperature. In pure Zr, hydride nucleation can be easily triggered in an electron-polished sample by electron beam irradiation [23]. Post-precipitation EBSD analysis can be used to analyze the characteristics of low-angle grain boundaries (LAGBs) and high-angle grain boundaries (HAGBs), as well as the orientation of Zr matrix. Using this method, we conducted a systematic investigation into the nucleation and precipitation of intergranular hydrides in Zr. A thermodynamic model is also proposed to rationalize the precipitation of needle-shaped hydrides at GB. The correlation between GB character and intergranular hydrides is discussed.

2. Experimental methods

2.1. Sample preparation

High-purity Zr (>99.99 wt.%) with low quantities of trace elements was used in this experiment. The Zr plate underwent cold rolling with a 23 % reduction and annealing at 600 °C for 8 h to achieve an equiaxed grain structure. The final average grain size is 5.19 μm (measured by EBSD). All samples subjected to heat treatments were sealed in an alundum tubular furnace (GSL-1400X) under a vacuum of less than 2×10^{-4} Pa. Thin foils for TEM observation were first cut from the bulk piece and mechanically ground to a final thickness of 50 μm, and subsequently electro-polished using a solution of 10 % perchloric acid in ethanol at a voltage of 25 V at −30 °C for 5 min. After electro-polishing, the samples were repeatedly dipped in the alcoholic solution to remove the residual acidic liquid and then transferred into TEM for in-situ observation.

2.2. In-situ observation inside TEM

In-situ observation experiments were carried out using a double-tilt holder inside a JEOL 2100F TEM at room temperature. The selected area with a thickness of 130±20 nm was irradiated by a 200 kV electron beam with a beam density of 20 pA cm^{-2} during the in-situ observation. After being exposed to the electron beam for a few seconds, hydrides begin to nucleate in Zr [23]. Real-time hydride nucleation and growth were recorded by a charge-coupled device camera at 10 frames per second. More than 10 samples were explored using this method. The sample thickness was obtained by measuring cross-sectional thickness in a scanning electron microscope (SEM) after TEM and EBSD characterization.

2.3. Microstructure characterization

After hydride precipitation, the morphology of intergranular hydrides was characterized by TEM. The orientation of grains and the crystallographic plane of GBs were determined based on the selected area diffraction patterns (SADF). Once the GB plane was determined, the α_{GB-BP} between the GB normal and [0001] direction (α_{GB-BP}) was calculated with the assistance of the CrystalMaker software. GB characteristics were determined by EBSD in the FEI Helios NanoLab dual-beam system with an Oxford Nordlys detector. The EBSD scans utilized an electron beam with an accelerating voltage of 30 kV and a probe current of 2.7 nA with a step size of 130~185 nm. The inverse pole figure (IPF) and crystal orientation were post-processed using Channel 5 software and Aztec HKL software. The misorientation and tilt axes were determined from the Euler angles of adjacent grains. LAGBs are defined as the GBs with a misorientation angle between 0° and 15°, and HAGBs refer to the GBs with a misorientation angle above 15° More than 140 GBs were analyzed regarding to GB plane, interacting angle between GB and BP (α_{GB-BP}), and misorientation angle-axis pair. Selected GBs with the same rotation axis are listed in Table 1.

3. Results

3.1. Morphology of hydrides

Fig. 1(a) shows the representative microstructure of the

Table 1
Hydride precipitation on GBs with different rotation axes and angles.

| Rotation axis	Rotation angle (°)	Hydride precipitation
<$10\bar{1}0$>	85.77	Type-a
<$10\bar{1}0$>	19.56/44.84/77.36/73.7/79.43	Type-b
<$10\bar{1}0$>	55.2	No hydrides
<$2\bar{1}\bar{1}0$>	38.43//61.74	Type-a
<$2\bar{1}\bar{1}0$>	34.27/35.37/80.77/89.4	Type-b
<$2\bar{1}\bar{1}0$>	27.59/51.7	No hydrides
<$8\bar{4}\bar{4}3$>	13.66/39.13/52.48/53.89	Type-a
<$8\bar{4}\bar{4}3$>	17.28/20.25/21.98/29.61	Type-b
<$8\bar{4}\bar{4}3$>	55.26/56.11/61.57	No hydrides
<$7\bar{2}\bar{5}3$>	26.91/31.84/49.79/57.7	Type-a
<$7\bar{2}\bar{5}3$>	44.09/60.65/65.96/69.56/71.24/72.5	Type-b
<$7\bar{2}\bar{5}3$>	5.07/12.93/25.02	No hydrides
<$7\bar{2}\bar{5}0$>	12.99/24.18/26.05	Type-a
<$7\bar{2}\bar{5}0$>	21.13/33.04/38.94/44.36/51.0978.51//89.18	Type-b
<$7\bar{2}\bar{5}0$>	16.28/21.88/57.81	No hydrides
<$5\bar{1}\bar{4}0$>	73.9	Type-a
<$5\bar{1}\bar{4}0$>	7.71/82/89.75	Type-b
<$5\bar{1}\bar{4}0$>	77.86/82.12	No hydrides
<$5\bar{1}\bar{4}3$>	28.44/34.22/57.97	Type-a
<$5\bar{1}\bar{4}3$>	41.87	Type-b
<$5\bar{1}\bar{4}3$>	37.36/53.14/57.18	No hydrides
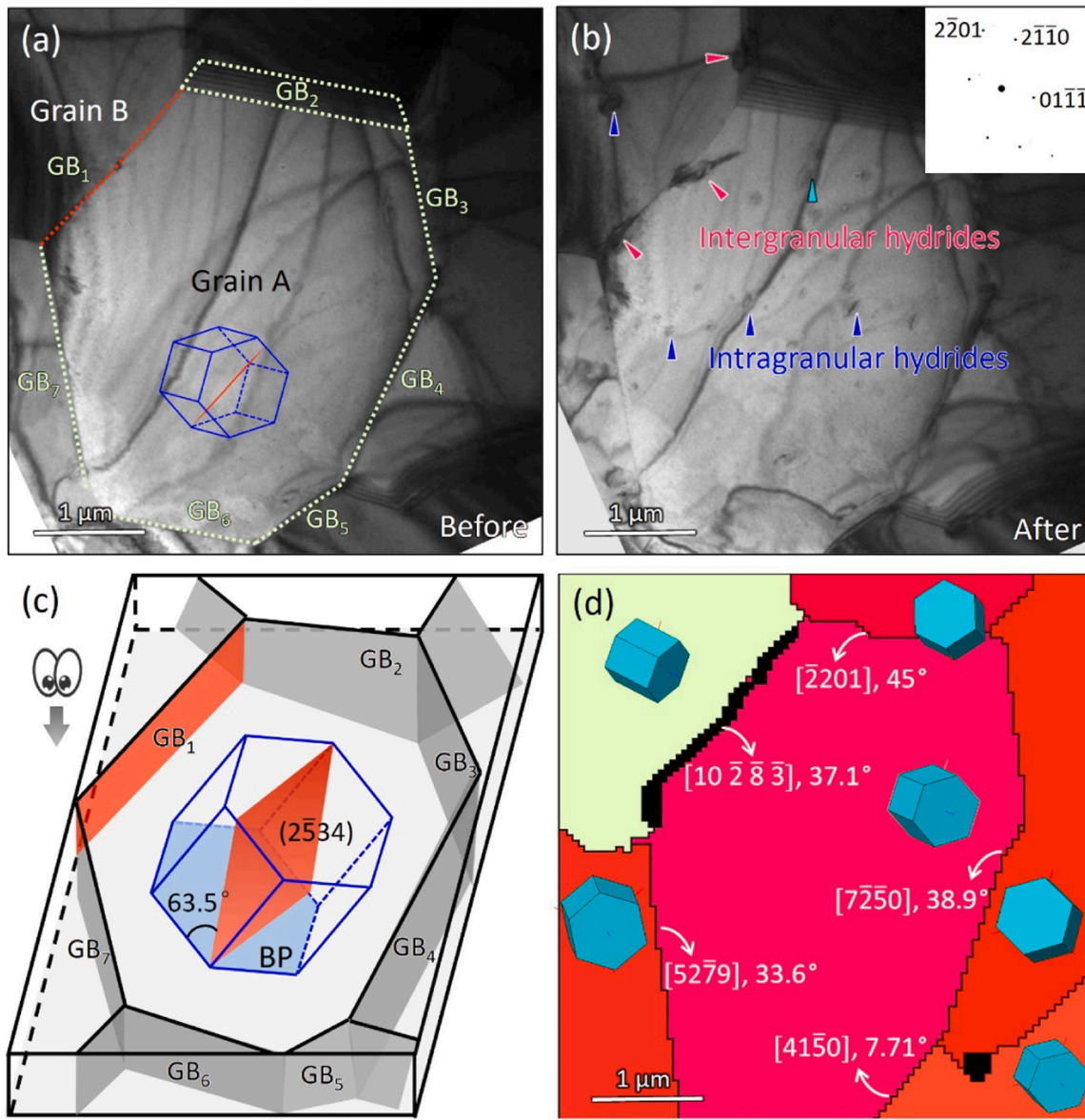
Fig. 1. In-situ observation of the hydride precipitation in recrystallized pure Zr and their correlation with grain boundary (GB) characteristics. (a) No hydrides and dislocations inside grains and on the GBs before electron-beam irradiation. (b) In-situ observation of intergranular and intragranular hydride nucleation after electron-beam irradiation. (c) Determination of Miller indices of GB plane and intersection angle between GB and BP. (d) Misorientation angle and rotation axes of GB according to EBSD scan.

recrystallized high-purity Zr. The initial microstructure is free of hydrides and dislocations. After 20 s of electron beam irradiation, several hydrides precipitate within grain A. Two larger hydrides nucleate at the GB$_1$, one growing along the GB and the other growing from the GB into the grain A, as shown in Fig. 1(b) and Movie S1. No hydrides are detected on GB$_2$ to GB$_7$. In order to determine the GB plane, the sample is tilted to make the GB plane with an edge-on position [24]. When the GB$_1$ plane is on the edge-on position, the beam direction is parallel to the [01$\bar{1}$2] direction of grain A, as indicated by the diffraction pattern in Fig. 2(b). Crystallographic analysis indicates that the GB$_1$ is parallel to the (2$\bar{5}$34) plane in grain A. Fig. 1(c) plots the orientation of the GB$_1$ plane in an HCP lattice. The α_{GB-BP} between the GB$_1$ plane and the basal plane (BP) is 63.5° The misorientation angle between grain A and grain B is 37.1° The details of grain orientations, misorientation angles, and tilting axes of GB$_2$-GB$_7$ are shown in Fig. 1(d).

Fig. 2a shows the morphology of two types of intergranular hydrides when the GB is in the top-view position. The hydrides lying on GB are marked as *type-a*, while those hydrides growing from GB into grain are named *type-b*. Type-b hydrides have the same habit plane (0001) and growth direction <2$\bar{1}$10> as the intragranular hydrides, as indicated by the diffraction pattern in Fig. 2(a$_2$). The sample is tilted 24° to make the GB plane parallel to the beam direction (Fig. 2(b$_1$)). According to the diffraction pattern in Fig. 2(b$_2$) and Fig. 2(b$_3$), the GB is not parallel to the (0001) plane of any adjacent grains. Type-a hydride is close to the grain A side of the GB. The tips of type-a hydride are surrounded by dislocations [23]. In this study, type-a or type-b hydrides on the GBs can be easily determined according to their morphologies. See details in Table 1.

3.2. Intergranular hydrides at LAGBs

Twelve LAGBs are detected and the hydride precipitation on parts of these LAGBs are shown in Fig. 3. The IPF maps in Fig. 3(a$_1$) to Fig. 3(a$_6$) display the orientation of grains and GB misorientation angles. Fig. 3
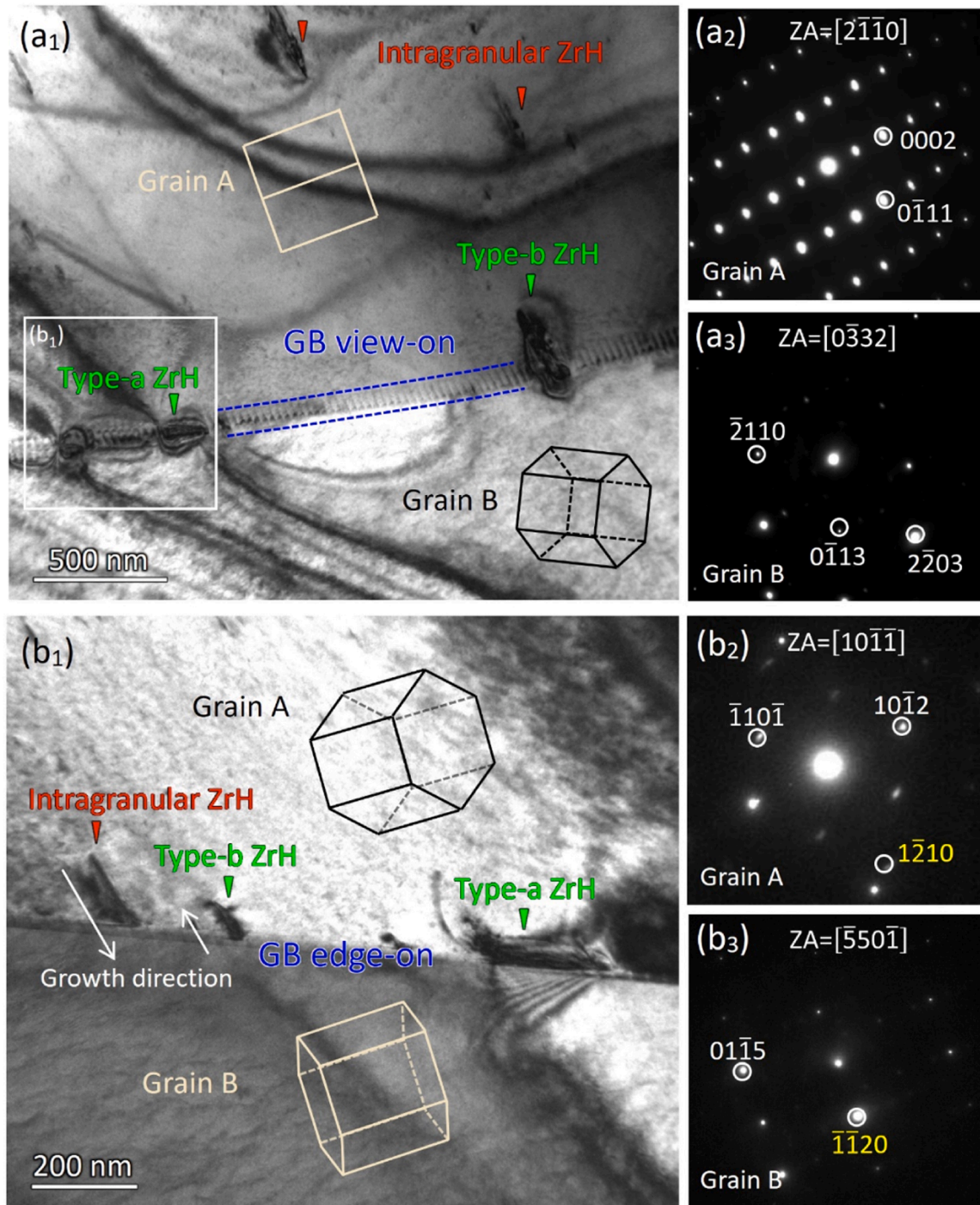
Fig. 2. TEM images showing the morphology of the intergranular and intragranular hydrides. (a₁) Type-a and type-b hydrides on a GB with top-view position. (a₂) Diffraction pattern of grain A in (a₁). (a₃) Diffraction pattern of grain B. (b₁) Enlarged images showing type-a and type-b hydrides on the same GB with edge-on position. (b₂) Diffraction pattern of grain A in (b₁). (b₃) Diffraction pattern of grain B in (b₁).

(b₁-b₆) shows the types of hydrides at LAGBs after precipitation. Nano-sized hydrides nucleate near the GB when the GB misorientation is 4.4°, as shown in Fig. 3(b₁) and Movie S2. No further hydrides nucleate on this GB thereafter. Further, no hydrides form on GBs with misorientation angles of 5.5° and 13°, as shown in Fig. 3(b₂) and Fig. 3(b₅). Instead, some intragranular hydrides nucleate in the interior of the grain in Fig. 3 (b₅). Type-b hydrides were observed when the GB misorientation angle is 10° and 11.4°, as shown in Fig. 3(b₃) and Fig. 3(b₄). For a GB misorientation angle of 13.5°, both type-a and type-b hydrides precipitate, as shown in Fig. 3(b₆). The crystallographic planes of GBs in Fig. 3

are determined and marked by white dashed lines in Fig. 3 (b₁-b₆). The α_{GB-BP} between the GB and BPs of two adjacent grains are also calculated. The calculated α_{GB-BP} and crystallographic plane for each LAGB are listed in Table 2.

Specific crystallographic planes are thought to be the preferred nucleation sites for intergranular hydrides [11,12]. Here, we project the normal of all the LAGB planes in an IPF map in Fig. 4(a), which reflects the relationship between the GB planes and the specific crystallographic planes, such as (0001), {10$\bar{1}$0} and {$\bar{2}$110}. The GB planes of two adjacent grains are labeled with the same color and with a rod
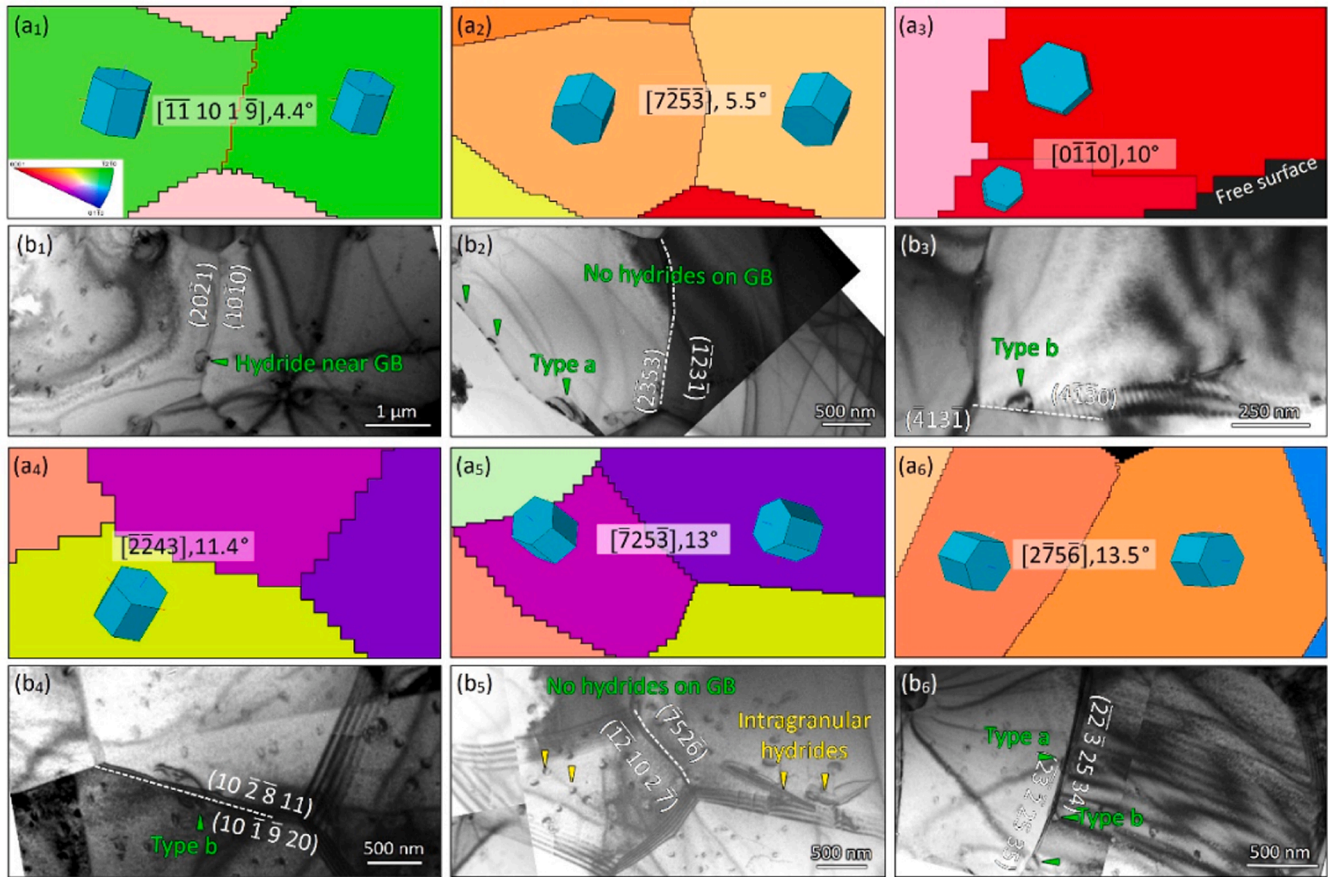
Fig. 3. Hydride precipitation at SAGBs with different axis-angle pairs: (a₁) [$\overline{11}$ 10 1 $\overline{9}$],4.4°, (a₂)[$7\overline{2}5\overline{3}$], 5.5°, (a₃)[$0\overline{1}\overline{1}0$],10°, (a₄)[$\overline{2}\overline{2}43$],11.4°, (a₅) [$\overline{7}25\overline{3}$],13° and (a₆)[$2\overline{7}5\overline{6}$],13.5° TEM images showing hydride precipitation at the SAGBs with various crystallographic planes. (b₁) A small hydride precipitated near the GB. (b₂) No hydrides precipitate on the GB. (b₃) Type-a hydrides precipitate on the GB. (b₄) Type-b hydrides precipitate on the GB. (b₅) No hydrides precipitate on the GB. (b₆) Both type-a and type-b hydrides precipitate on the GB. Numbers in white parentheses mark the crystallographic planes.

Table 2
Characteristics of SAGBs with hydride precipitation in Fig. 3.

GB No.	Rotation vector (axis/angle)	GB plane	$\alpha_{\text{GB-BP}}(°)$	Hydride precipitation
1	[$\overline{11}$ 10 1 $\overline{9}$]/4.38°	($20\overline{2}1$)//($10\overline{1}0$)	75.39/76.4	No hydrides
2	[$25\overline{7}9$]/4.94°	($30\overline{3}2$)//($\overline{13}$ $\overline{60}$ 73 48)	70.1/68.8	No hydrides
3	[$52\overline{7}3$]/5.07°	($01\overline{1}0$)//($05\overline{5}1$)	90/83.7	No hydrides
4	[$\overline{7}25\overline{3}$]/5.51°	(2 $\overline{15}$ 13 1)//($\overline{20}$ 7 27 $\overline{24}$)	87.8/74.8	No hydrides
5	[$41\overline{5}0$] /7.71°	(11 $\overline{15}$ 4 12)//($\overline{10}$ 5 5 9)	60.2/74.2	No hydrides
6	[$\overline{2}3\overline{1}0$] /9.26°	($\overline{5}$ 10 $\overline{5}$ 4)//($\overline{9}$ 8 17 2)	75.4/82.3	No hydrides
7	[$\overline{7}25\overline{3}$]/12.93°	($\overline{7}52\overline{6}$)//($\overline{12}$ 10 2 $\overline{7}$)	62.4/71.1	No hydrides
8	[$5\overline{4}112$]/13.87°	($\overline{2}353$)//($\overline{1}23\overline{1}$)	69.5/73	No hydrides
9	[$\overline{7}250$]/12.99°	($0\overline{1}12$)//($0\overline{2}26$)	42.6/31.5	Type-a
10	[$0\overline{1}\overline{1}0$] /10°	($4\overline{1}30$)//($\overline{4}13\overline{1}$)	90/81.4	Type-b
11	[$\overline{2}243$]/11.4°	(10 $\overline{1}$ $\overline{9}$ 20)//(10 $\overline{2}$ $\overline{8}$ 11)	41.3/56.8	Type-b
12	[$2\overline{7}5\overline{6}$]/13.51°	($\overline{23}$ $\overline{2}$ 25 35)//($\overline{22}$ $\overline{3}$ 25 34)	51.7/51.3	Type-b

connection. The numbers labeled on the circles correspond to the GBs listed in Table 2. No hydrides are observed on GBs labeled 1–8 (see gray circles). Either type-a or type-b hydrides precipitate on GBs with numbers of 9–12 (see blue circles). We found no fixed relationship between the hydride precipitation and specific crystallographic planes. The relationship between hydride types and the LAGB misorientation angles is plotted in Fig. 4b. No intergranular hydrides are detected when the LAGB misorientation angle is less than 10°. When the misorientation angle becomes larger, either type-b or type-a hydrides precipitate. Fig. 4c further highlights the hydride precipitation versus the $\alpha_{\text{GB-BP}}$. Most GBs with $\alpha_{\text{GB-BP}}$ between 60° and 90° have no hydride

precipitation. Type-b hydrides form on the GB with $\alpha_{\text{GB-BP}}$ between 30° and 60° Only one type-a hydride is detected and the $\alpha_{\text{GB-BP}}$ is nearly 30° (Fig. 3(b₆)). Hydride nucleation on LAGBs depends on both the misorientation angle and the $\alpha_{\text{GB-BP}}$. A misorientation angle between 10° and 15° or the $\alpha_{\text{GB-BP}}$ less than 60° is favorable for the intergranular hydride.

3.3. Intergranular hydrides at HAGBs

Fig. 5 displays the precipitation of intergranular hydrides on HAGBs with [$0\overline{1}10$] rotation axis at different misorientation angles. At the misorientation angles of 19.6°, 44.8°, 77.4° and 79.4°, type-b hydrides
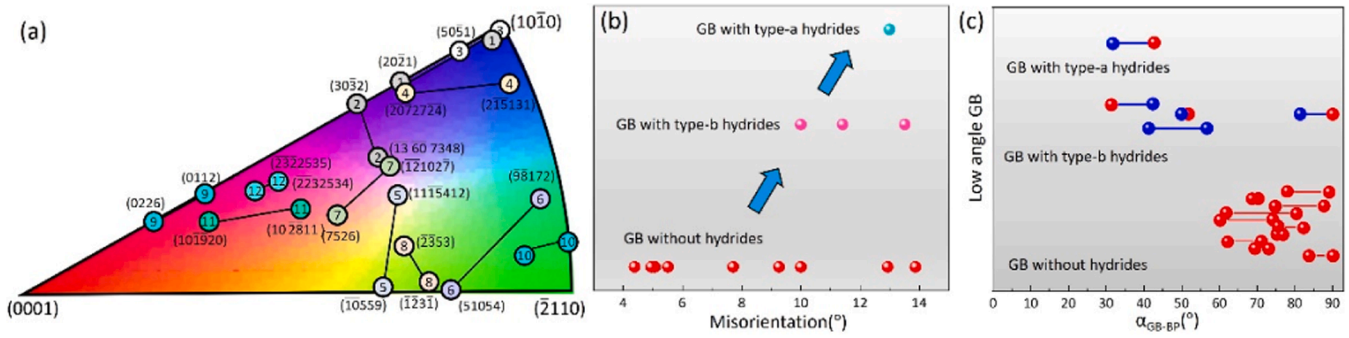
Fig. 4. (a) SAGB plane orientations in an IPF map: the same number represents GB planes of two adjacent grains. Statistical analysis of hydrides at SAGBs as a function of (b) axis misorientation and (c) α_{GB-BP}. Blue circles in (c) mean the GB side with hydrides and red circles stand for the GB side free of hydrides.
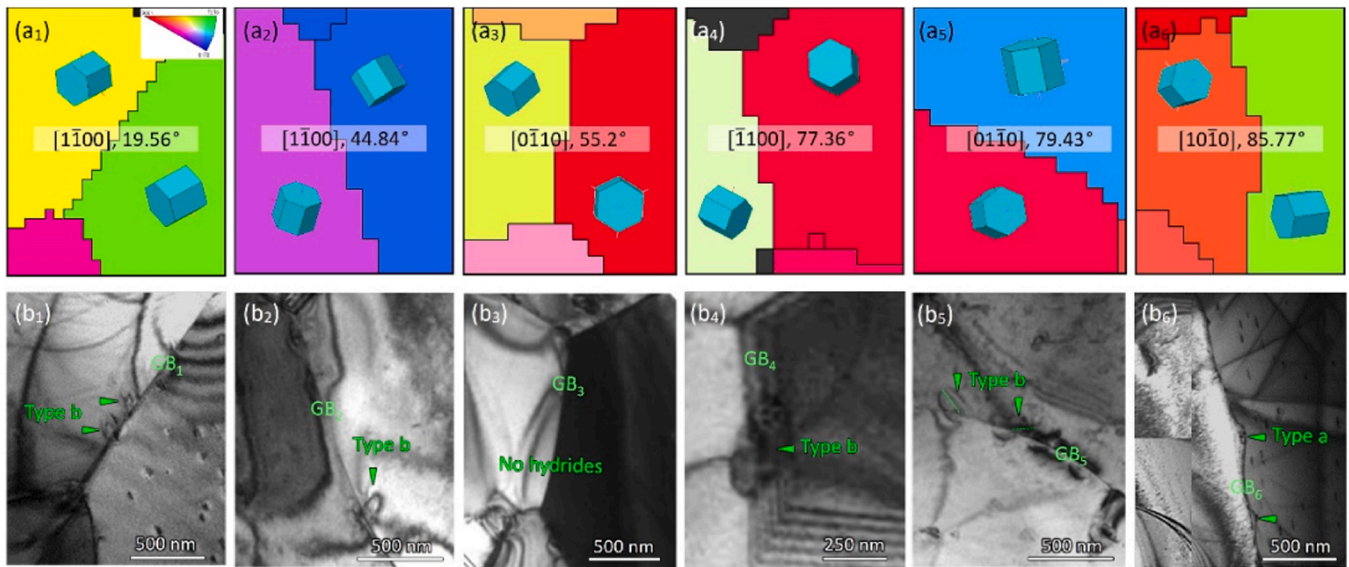

Fig. 5. Hydride precipitation at HAGBs with [$1\bar{1}00$] rotation axis and different rotation angle: (a_1) 19.56°, (a_2) 44.84°, (a_3) 55.2°, (a_4) 77.36°, (a_5) 79.43° and (a_6) 85.77° The corresponding TEM images showing hydride precipitation at GBs. (b_1) Type-b hydrides on GB$_1$. (b_2) Type-b hydrides on GB$_2$. (b_3) No hydrides on GB$_3$. (b_4) Type-b hydrides on GB$_4$. (b_5) Type-b hydrides on GB$_5$. (b_6) Type-a hydrides on GB$_6$.

are formed on GBs, as shown in Fig. 5(b_1), Fig. 5(b_2), Fig. 5(b_4) and Fig. 5(b_5)). No hydrides are detected on the GBs with a misorientation angle of 55.2° (Fig. 5(b_3)), where the α_{GB-BP} of two adjacent grains are 63.6° and 89°, respectively. At the misorientation angle of 85.8°, type-a hydrides precipitate along the GBs (Fig. 5(b_6)). Similarly, the HAGBs with [$2\bar{1}\bar{1}0$] rotation axis are displayed in Fig. 6. No hydrides are found on the GBs with the misorientation angles of 27.6 ° and 51.7° (Fig. 6(b_1)) and (b_4). For misorientation angles of 34.3 ° and 80.8°, type-b hydrides form on the GBs, as shown in Fig. 6(b_2) and Fig. 6(b_6)). Some dislocations are emitted from the hydride tip and wrap around the hydride (see Fig. 6(b_2) and Movie S3). A stress field contrast is generated on the other side of the GB (Fig. 6(b_2) and Fig. 6(b_6)). Type-a hydrides formed on GBs have misorientation angles of 38.4° and 62.2°, as displayed in Fig. 6(b_3) and Fig. 6(b_5)). No clear correlation is observed between the misorientation angle of HAGBs and the nucleation of intergranular hydrides.

The interacting angles between BPs and HAGBs with rotation axes [$0\bar{1}10$] and [$2\bar{1}\bar{1}0$] are determined, as shown in Fig. 7. There is a close relationship between hydride precipitation and the α_{GB-BP}. For GBs with [$0\bar{1}10$] rotation axis, intergranular hydrides prefer to nucleate on GBs with α_{GB-BP} less than 70° When α_{GB-BP} is less than 39°, the GB prefers to form type-a hydrides, while the GB forms type-b hydrides when α_{GB-BP} falls between 39° and 70°. The GBs are free of hydrides when the α_{GB-BP} is greater than 70°. A similar trend is also found for GBs with [$2\bar{1}\bar{1}0$]

rotation axis. Type-a hydrides are preferentially formed on GBs with α_{GB-BP} less than 40°. Type-b hydrides are formed on GBs with α_{GB-BP} between 40° and 60°. No hydride forms on GBs with α_{GB-BP} larger than 60° (Fig. 7 (b)). In short, intergranular hydride nucleation on HAGBs depends on α_{GB-BP}. The remaining HAGBs in Table 1 are also analyzed in terms of α_{GB-BP}. The distribution exhibited an analogous trend to that depicted in Fig. 7.

4. Discussion

4.1. Thermodynamic model of needle-shaped hydride precipitation

According to in-situ TEM observations (Movie S1), two distinct needle-shaped intergranular hydrides are identified (Fig. 1 and Fig. 2). The formation of type-a or type-b hydride depends on the α_{GB-BP} according to the statistical analysis in Fig. 4 and Fig. 7. To assess the effect of the α_{GB-BP} on the precipitation of intergranular hydrides, a thermodynamic-based nucleation model is proposed. The effect of GB characteristics on the nucleation of plate-shaped δ hydrides has been described in previous research [25]. The model of the intergranular δ-hydrides nucleus is based on a spherical precipitate without considering the surface energy anisotropy of the hydride [25–27]. However, the shape of the precipitate (spheroid, needle, or plate) determines the kinetic factor of nucleation [28,29]. Here, we developed a
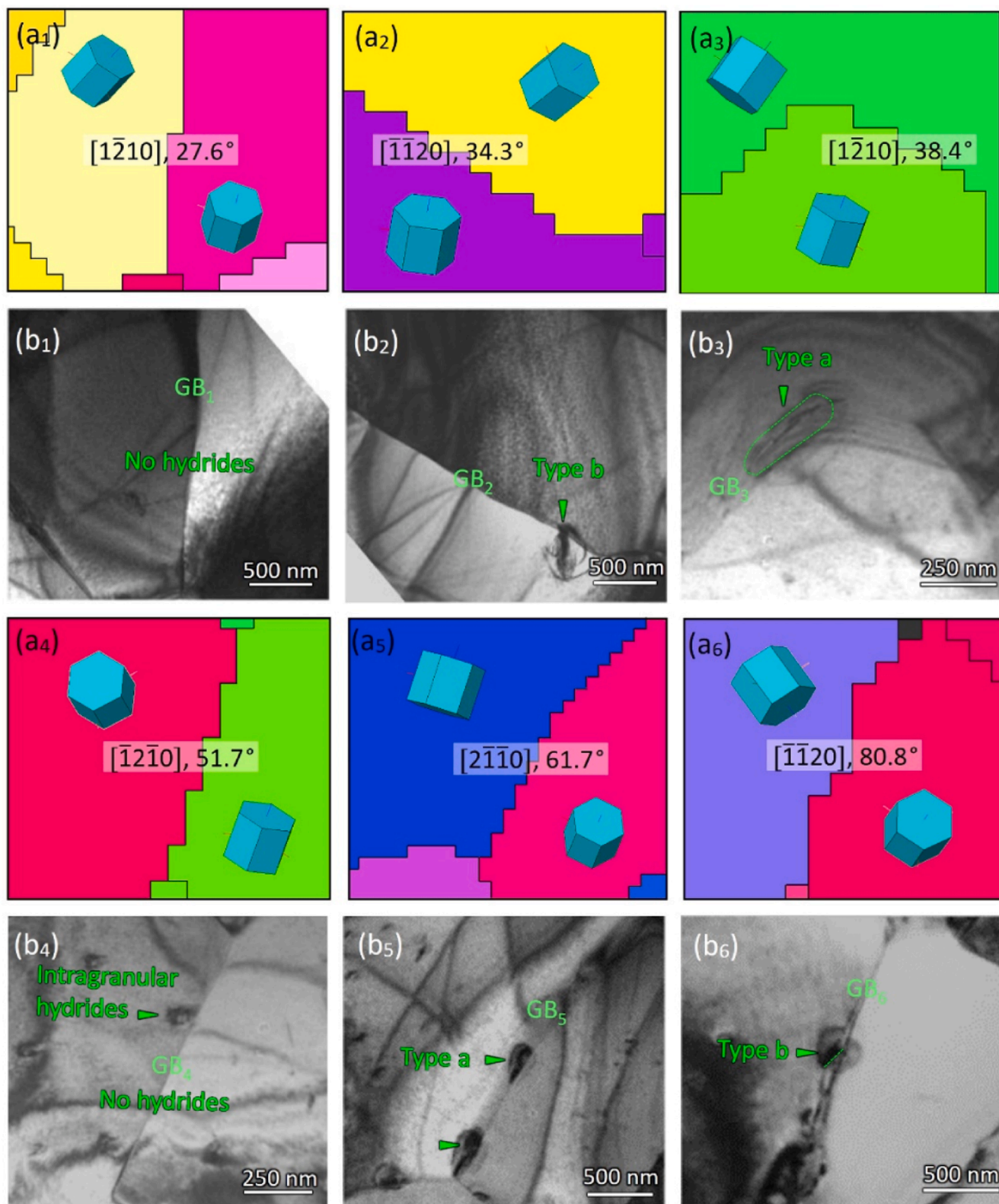
Fig. 6. Hydride precipitation at HAGBs with $[\bar{1}2\bar{1}0]$ rotation axis and different rotation angle: (a$_1$) 27.6°, (a$_2$) 34.3°, (a$_3$) 38.4°, (a$_4$) 51.7°, (a$_5$) 61.7° and (a$_6$) 80.8° The corresponding TEM images showing hydride precipitation at GBs. (b$_1$) No hydrides on GB$_1$. (b$_2$) Type-b hydrides on GB$_2$. (b$_3$) Type-a hydrides on GB$_3$. (b$_4$) No hydrides on GB$_4$. (b$_5$) Type-a hydrides on GB$_5$. (b$_6$) Type-b hydrides on GB$_6$.
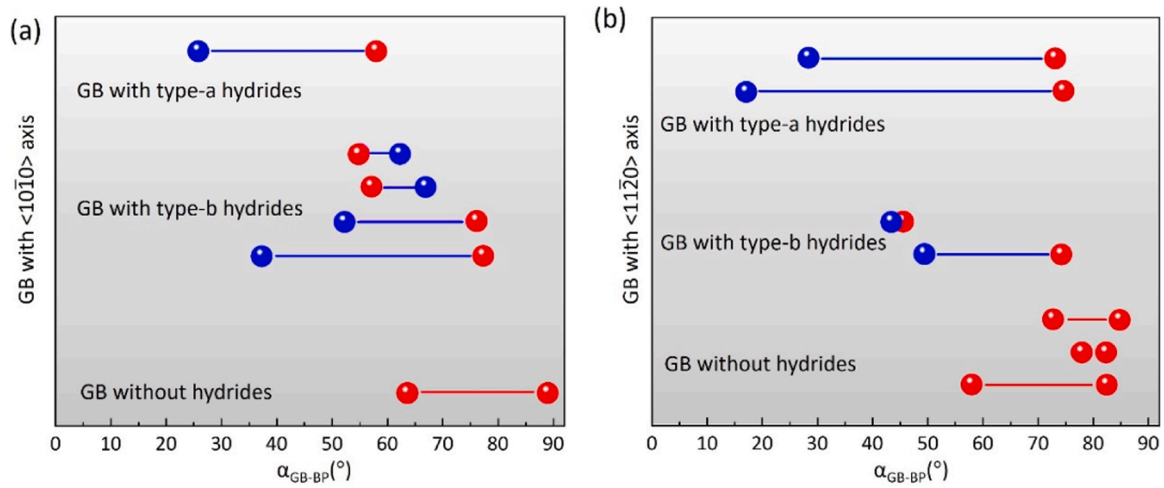
Fig. 7. Analysis of hydrides at HAGBs with (a) $[1\bar{1}00]$ rotation axis and (b) $[\bar{1}2\bar{1}0]$ rotation axis as a function of $\alpha_{GB\text{-}BP}$. Blue circles represent the GB side with hydrides and red circles stand for the GB side free of hydrides.

thermodynamic model to describe the nucleation of needle-shaped γ-hydride according to experimental observations.

Fig. 8(a) shows the typical morphology of needle-shaped intragranular hydride according to TEM observations, type-a and type-b intergranular. The schematics of the three types of hydrides are plotted in Fig. 8(b). The formation energy of the hydride nucleus ΔG is given by [29]:

$$\Delta G = \Delta G_v + \Delta G_s - \Delta G_{GB}/\Delta G_{vac} \tag{1}$$

which is composed of three terms: the contribution of the bulk free energy of transformation ΔG_v, including the chemical free energy for nucleation from solid solution and the elastic strain energies, the
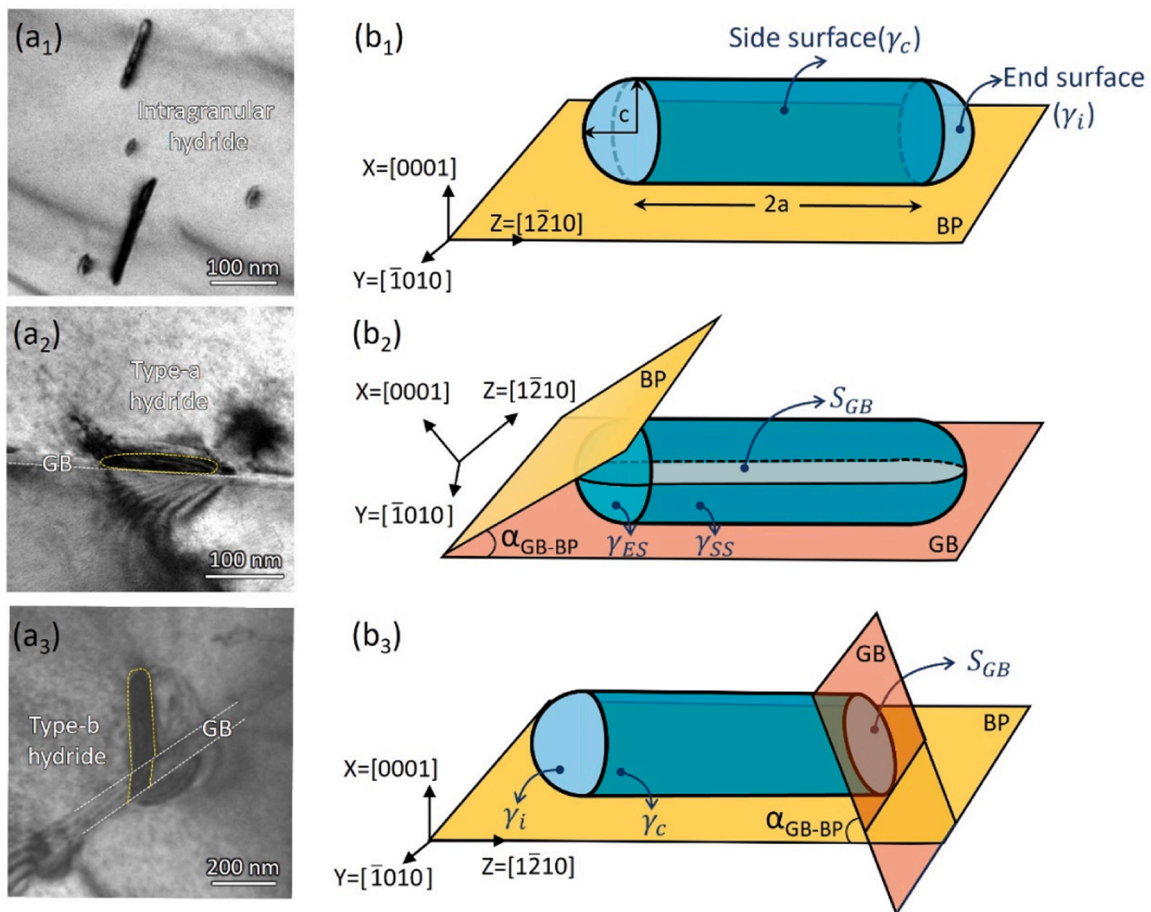

Fig. 8. The shape of intragranular and intergranular hydride nuclei. (a_1) Intragranular hydrides, (a_2) Intergranular hydrides growing along GB (type-a), and (a_3) Intergranular hydrides growing from GB to parent grain (type-b). (b_1) Model of needle-shaped intragranular hydrides lying on the basal plane. (b_2) Model of type-a hydride lying on the GB. (b_3) Model of type-b hydride lying on the basal plane and interacting an angle $\alpha_{GB\text{-}BP}$ with GB.

interfacial energy ΔG_s between the matrix and the hydrides, and the energy provided by nucleation sites such as ΔG_{GB} for GBs or ΔG_{vac} for vacancy clusters.

For intragranular hydrides, the long axis is parallel to the $<11\bar{2}0>$ direction of the Zr matrix. We assume the tip of the needle-shaped hydride is a hemispheroid, and the middle part of the hydride is a cylinder, with radius c and length $2a$, as illustrated in Fig. 8(b_1). The area of the hydride side surface is $S_{ss} = 4\pi ac$, and the area of hydride end surface is $S_{ES} = 2\pi c^2$. In this way, the calculation of the total interfacial energy can be simplified [27]. According to the HR-TEM characterization of the interface between the hydride and the matrix [23], the two end faces associated with the production of dislocations are incoherent and have a specific interfacial energy γ_i. While the surface of the cylinder along the long axis remains semi-coherent with the matrix and has an interfacial energy γ_c [23,27–30]. The total free energy ΔG for the heterogeneous nucleation of intragranular hydride with volume $V = \frac{4}{3}\pi c^3 + 2\pi ac^2$ can be expressed as [27]:

$$\Delta G_{intra} = V(\Delta g_{strain} - \Delta g_{chem}) + 4\pi ac\gamma_c + 4\pi c^2\gamma_i \tag{2}$$

where Δg_{chem} is the absolute value of the Gibbs free energy of transformation per unit volume, Δg_{strain} is the elastic strain energy per unit volume due to lattice mismatch and can be estimated by $\Delta g_{strain} = \frac{6\mu\alpha\gamma\varepsilon^2}{\alpha(\gamma-1)+1}$ [25], where $\alpha = (1+\upsilon)/3(1-\upsilon)$, μ is the shear modulus (33.82 GPa), υ is Poisson's ratio, γ is the ratio of the bulk modulus of the hydride to that of the matrix (γ=12/13.5), and ε is the misfit strain between the

hydride and matrix. In the absence of additional hydrogen charging and relaxation of the sample surface, Δg_{chem}=1.649 × 10^8 J/m^3 and Δg_{strain} =1.236 × 10^8 J/m^3 for pure Zr without external stress [25]. The critical dimension of the nucleus a_k and c_k is a result of surface energy term dominance, which yields [27]:

$$a_k = -\frac{3\gamma_i}{\Delta g_{strain} - \Delta g_{chem}} \tag{3}$$

$$c_k = -\frac{3\gamma_c}{\Delta g_{strain} - \Delta g_{chem}} \tag{4}$$

where the γ_c is set to 0.05 J/m^2 and γ_i equals 0.5 J/m^2 based on interfacial energy calculations [20,25]. One can obtain $a_k = 36$ nm and $c_k = 3.6$ nm.

For type-a hydrides, the long axis is parallel to the GB plane (Fig. 8 (a_2)). The hydrides on GBs have higher interfacial energy because they have no fixed orientation relationship with both neighboring grains. Assuming that the interfacial energy of type-a hydride can be divided into a coherent part and an incoherent part according to the α_{GB-BP}, thus the end surface energy γ_{ES} of type-a hydride can be expressed by ($\gamma_i cos\alpha_{GB-BP} + \gamma_c sin\alpha_{GB-BP}$), while the side surface energy γ_{SS} along the long axis is ($\gamma_i sin\alpha_{GB-BP} + \gamma_c cos\alpha_{GB-BP}$) [31]. The variation of γ_{ES} and γ_{SS} as a function of α_{GB-BP} are plotted in Fig. 9(a), ranging from 0.05 J/m^2 to 0.5 J/m^2. When $\alpha_{GB-BP} = 0°$, $\gamma_{ES} = \gamma_i$ and $\gamma_{SS} = \gamma_c$. The contact area between hydride and GB is $S_{GB} = (4ac + \pi c^2)$ according to Fig. 8(a_2). The GB strain energy is assumed to be the same for different types of GB because the surface relaxation relief parts of misfit strain reduce their
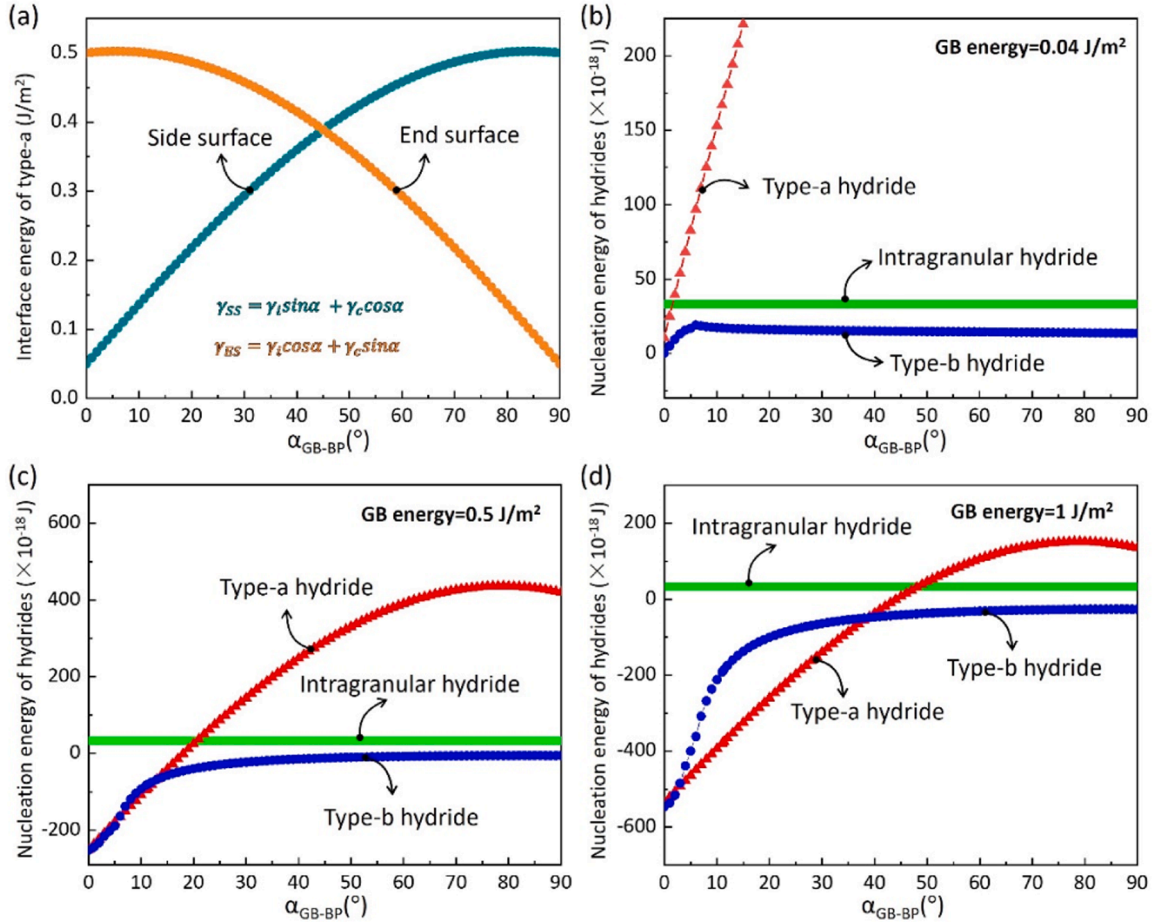

Fig. 9. Formation energy for intragranular and intergranular hydrides. (a) Variation of the surface energy of type-a hydride with the interacting angle between BP and GB. Nucleation energy of the intragranular and intergranular hydrides with GB energy of (b) 0.04 J/m^2 for SAGB, (c) 0.5 J/m^2 and (d) 1 J/m^2 for LAGB, respectively.

difference, thus we used the same strain energy for all hydrides either on GBs or in the interior of the grain [27]. Therefore, the total free energy for type-a hydrides can be expressed as:

$$\Delta G_{type-a} = V\left(\Delta g_{strain}^{GB} - \Delta g_{chem}\right) + 4\pi ca\gamma_{SS} + 4\pi c^2\gamma_{ES} - S_{GB}\gamma_{GB} \qquad (5)$$

where γ_{GB} is the GB energy.

For type-b hydrides, the long axis is parallel to the $<11\bar{2}0>$ direction, which is the same as intragranular hydrides. Therefore, the surface energy along the long axis is γ_c. According to the projection of type-b hydride on the inclined GBs in Fig. 8(a$_3$), the intersecting surface between hydride and GB is simplified as an ellipse in the model, as shown in Fig. 8 (b$_3$). The contact area is $S_{GB} = \frac{\pi c^2}{sin\alpha_{GB-BP}}$ when $\alpha_{GB-BP} \geq arctan\frac{c}{a}$ and $S_{GB} = \frac{a}{cos\alpha_{GB-BP}}\left(2\sqrt{c^2 - (atan\alpha_{GB-BP})^2} + 2c\right)$ when $\alpha_{GB-BP} < arctan\frac{c}{a}$. The energy of elliptical end surface γ_{ES} can be written as ($\gamma_i sin\alpha_{GB-BP} + \gamma_c cos\alpha_{GB-BP}$) because the interface between the hydride and GB is expected to be incoherent [31]. Assuming that the type-b hydride has a same critical nucleus volume as type-a and intragranular hydride, the side surface area S_{SS} is expressed as ($\frac{4}{3}\pi c^2 + 4\pi ca$). Thus, the total free energy of type-b hydrides is:

$$\Delta G_{type-b} = V\left(\Delta g_{strain}^{GB} - \Delta g_{chem}\right) + S_{SS}\gamma_c + 2\pi c^2\gamma_i + S_{GB}(\gamma_{ES} - \gamma_{GB}) \qquad (6)$$

The energy of symmetric tilt LAGBs ranges from 0.04 J/m^2 to 0.5 J/m^2 and symmetric tilt HAGBs ranges from 0.5 J/m^2 to 1 J/m^2 with tilt axes [0001], [1$\bar{1}$00] and [1$\bar{2}$10] [32–35]. For a quantitative analysis, the LAGB energy is set to 0.04 J/m^2 and 0.5 J/m^2, and the HAGB energy is considered to be 1 J/m^2 in this study.

4.2. Effect of GB energy on intergranular hydride precipitation

Using the above model, the nucleation energy of three types of hydrides with different GB energy is calculated, as shown in Fig. 9(b) to (d). Intragranular hydrides have constant nucleation energy because their formation is independent of GB energy and GB characteristics. The nucleation energy of type-a and type-b hydrides increases with the enhancement of α_{GB-BP}. Both type-a and type-b hydrides have the same nucleation energy when $\alpha_{GB-BP}=0°$, where the GB plane is parallel to (0001). For LAGBs, when γ_{GB}=0.04 J/m^2 (Fig. 9(b)), the type-b hydride has a much lower nucleation energy than type-a hydrides, and a similar nucleation energy with intragranular hydrides. As γ_{GB} increases to 0.5 J/m^2 (Fig. 9(c)), the nucleation energies of type-a and type-b are almost equal when α_{GB-BP} is less than 15° When α_{GB-BP} is greater than 15°, type-b has lower nucleation energy than both intragranular and type-a hydrides. The model shows that type-b hydrides on LAGBs and intragranular hydrides are energetically favorable. Increasing the GB energy is beneficial to nucleate type-a hydrides. These predictions are consistent with the statistical results in Fig. 4(b).

When γ_{GB}=1 J/m^2 (Fig. 9(d)), the nucleation energy of intragranular hydrides becomes negative, suggesting that HAGBs with a higher energy promote intergranular hydride precipitation [17]. An α_{GB-BP} transition appears at 39° Below 39°, type-a hydrides have a lower nucleation energy than type-b hydrides, indicating that type-a hydrides prefer to form. Otherwise, type-b hydrides prefer to nucleate on the GB. Such regulation is consistent with our experimental observations in Fig. 5 to Fig. 7. Notably, when α_{GB-BP} is less than 5°, the nucleation energy of type-b is nearly the same as type-a hydrides because they have a similar contact area with the GB and interfacial energy. In practice, the strain energy on the GBs differs from that in the matrix. Therefore, the influence of varying strain energies on the nucleation of intergranular hydrides has been calculated in the same method. Our findings indicate that the above-mentioned conclusion remains valid when Δg_{strain}^{GB} varies from 3.9×10^6 J/m^3 to 1.5×10^8 J/m^3. The intragranular hydrides are assumed to nucleate homogeneously in the energy calculation. Hence the formation energy of intragranular hydrides is higher than that of

intergranular hydrides, as indicated by green lines in Fig. 9. In fact, vacancy clusters induced by electron beam irradiation promote the intragranular hydride nucleation [23,36,37]. In-situ experiments also show that many intragranular hydrides precipitate together with the formation of intergranular hydrides (see Movie S1). We believe that these phenomena are related to defect-mediated intragranular hydride precipitation.

4.3. Effect of GB character on intergranular hydride precipitation

4.3.1. Role of GB plane orientation

The orientation of the GB plane is one of the important factors affecting intergranular precipitation [38]. It has been reported that the hydrides tend to precipitate on GBs parallel to (0001) or (10$\bar{1}$i) ($i = 0\sim7$), which are common habit planes of the hydrides [12,13]. However, after plotting the orientations of LAGB planes in the IPF map (Fig. 4), the distribution of GB with hydride precipitation is found to be dispersive. For example, GB$_{10}$, GB$_{11}$, and GB$_{12}$ with random crystallographic planes have hydride precipitation. In the case of HAGBs, hydrides nucleate on the GB with any crystallographic plane. Therefore, the orientation of the GB plane does not appear to be a key factor in affecting intergranular hydride precipitation.

4.3.2. Role of misorientation angle

Based on the classical theory of Read and Shockley [39], the variation of GB energy as a function of the misorientation angle is assumed to be the reason that affects the nucleation of intergranular hydrides. GBs with higher misorientation are the regions of choice for hydride precipitation because they have higher energy [17,25]. This view is clear for the LAGBs in Fig. 4(b). No hydride is seen on GBs when the misorientation angle is less than 10°. Above 10°, both type-a and type-b hydrides appear. This tendency becomes less noticeable for HAGBs (Fig. 5 and Fig. 6). The structure of GB dislocation cores determines the energy of HAGBs. Due to a similar arrangement of discrete dislocations or zigzag-shaped dislocation core structure, the GB energy difference of HAGBs with large tilt angles is relatively minor in the energy calculation of GBs with [1$\bar{2}$10] and [0$\bar{1}$10] tilt axes [33,34]. It has been shown that the majority of HAGBs have intergranular hydride nucleation (Fig. 5 and Fig. 6). When the misorientation angle is close to 30° or 60° [34], some HAGBs with highly symmetric dislocation structures show energy cusp, which prevents hydride precipitation on GBs (see Fig. 5(a3), Fig. 6(a1) and (a4)). In a nutshell, the misorientation angle has a greater effect on the intergranular hydride nucleation on LAGBs than that on HAGBs.

4.3.3. Role of interacting angle between GB and BP (α_{GB-BP})

The α_{GB-BP} is believed to be a key factor affecting intergranular hydride precipitation based on statistical analysis (Fig. 4 and Fig. 7) and the thermodynamic calculations. Fig. 10 summarizes the relationship between α_{GB-BP} and hydride precipitation. Type-a hydrides nucleate and develop along the GB when α_{GB-BP} is less than 39° (Fig. 10(a)). Type-b hydrides tend to nucleate at the GBs and grow into the interior of the grains when α_{GB-BP} increases to 70° (Fig. 10(b)). Hydride precipitation is rarely seen at the GBs when α_{GB-BP} is close to 90° (Fig. 10(c) and Fig. 10 (d)). Phase interface energy and GB strain energies are the main inhibitors of hydride nucleation. Since type-b hydrides precipitate on BP and grow along the [1$\bar{2}$10] direction to minimize the elastic strain energy [40,41], so the hydride interface remains semi-coherent with Zr matrix [23]. The interface of type-a hydride is regarded as incoherent because it does not have a fixed orientation relationship with Zr matrix. The nucleation barrier of type-b hydrides is much smaller than type-a hydrides. When α_{GB-BP} is less than 39°, type-a hydride has smaller interfacial energy (Fig. 9(a)). Smaller interfacial energy and larger GB energy favor type-a hydride nucleation. When GB is parallel to the (11$\bar{2}$0) plane (Fig. 10(c)), the GB strain energy and interfacial energies of type-a hydrides are larger than those of type-b and intragranular
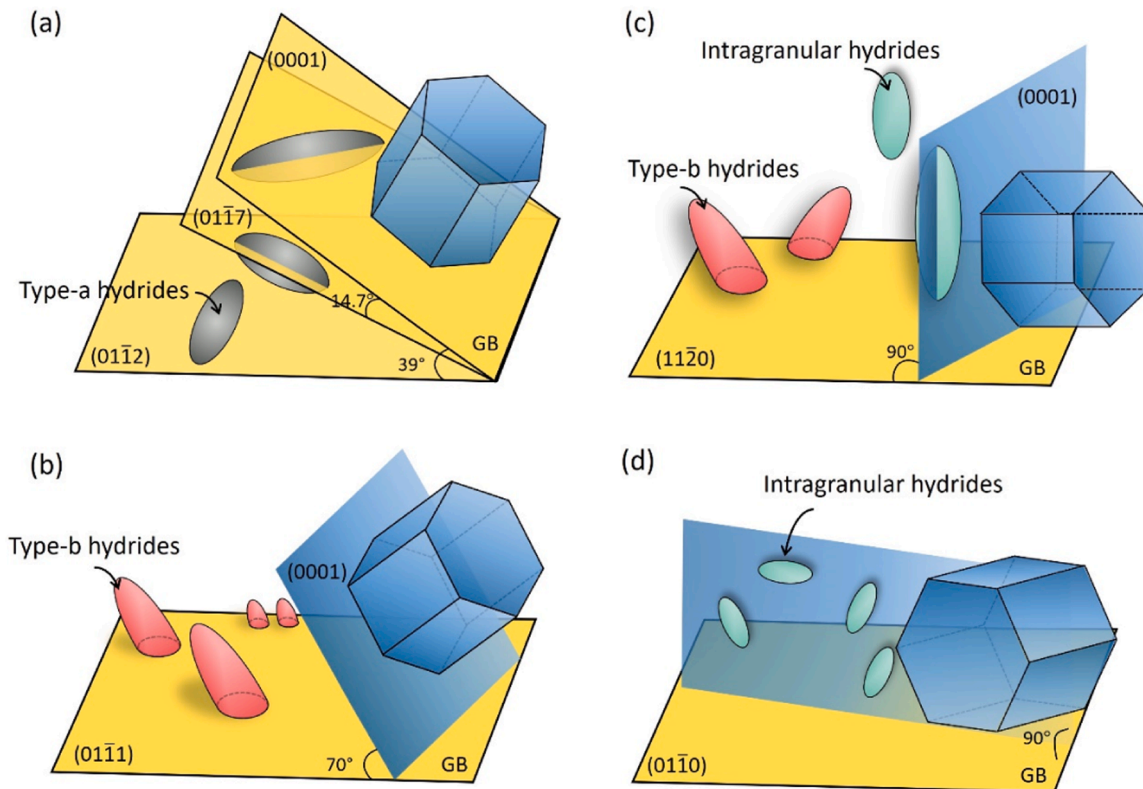
Fig. 10. Cartoons showing the relationship between intergranular hydrides and the α_{GB-BP}. (a) Type-a hydrides on GBs with α_{GB-BP} less than 39°. (b) Type-b hydrides on GB with α_{GB-BP} between 39° and 70°. (c) and (d) Intragranular hydrides dominate when GBs with α_{GB-BP} between 70° and 90°.

hydrides, providing more opportunities for the formation of intragranular hydrides or type-b hydrides. Based on these observations, we conclude that the GBs with α_{GB-BP} of two neighboring grains higher than 70° are resistant to hydride precipitation.

4.4. Effect of irradiation defects on intergranular hydride precipitation

Hydride nucleation in this study is stimulated by electron beam irradiation (see Movie S1). Vacancies (first form in ZrO and then transfer into Zr) induced by irradiation trap the solute hydrogen, resulting in intragranular hydride precipitation [23]. When GB is present, irradiation defects also affect the hydride precipitation as they are strong traps for point defects. Although most GBs are biased absorbers of the self-interstitial atoms, some asymmetric tilt GB can act as a sink for vacancies, such as the GB parallel to $(01\bar{1}2)$ [42–44]. Absorption of vacancies generates a tensile stress field on one side of the GB, which promotes hydrogen segregation as well and assists hydride precipitation [45]. This is consistent with the experimental results of type-a hydrides precipitation on the $(01\bar{1}2)$ GB (see Fig. 4(a)).

5. Conclusions

In this work, the precipitation of microscopic intergranular hydrides in pure Zr was investigated by in-situ TEM observations and EBSD characterizations. The influence of the characteristics of GBs on the nucleation of intergranular hydrides is analyzed. The main findings are as follow.

(1) Two different types of intergranular hydride were observed. Type-a hydrides grow along the GB, whereas type-b hydrides nucleate at GBs and grow into the grain interior. Type-b hydrides follow the same orientation relationship with Zr matrix as the intragranular hydrides, while type-a hydrides do not.

(2) The interacting angle between GB and BP (α_{GB-BP}) is a key factor in governing the hydride precipitation at the GBs. When α_{GB-BP} is less than 60°, type-b hydrides dominate at LAGBs, and no intergranular hydrides form if α_{GB-BP} is larger than 60°. For HAGBs, type-a hydrides tend to form on GBs when α_{GB-BP} is less than 39°. When α_{GB-BP} is between 39° and 70°, type-b hydrides prefer to form. Once α_{GB-BP} is higher than 70°, no intergranular hydride precipitation occurs.

(3) Type-a hydrides prefer to form on GBs with higher GB energies, which aggravates hydrogen embrittlement in Zr alloys. Therefore, one can try to introduce a high fraction of low-energy GBs to inhibit the precipitation of type-a hydrides.

CRediT authorship contribution statement

Si-Mian Liu: Conceptualization, Data curation, Formal analysis, Funding acquisition, Investigation, Methodology, Writing – original draft, Writing – review & editing. **Wei-Zhong Han:** Conceptualization, Formal analysis, Funding acquisition, Project administration, Resources, Supervision, Writing – original draft, Writing – review & editing.

Declaration of competing interest

The authors declare that they have no known competing financial interests or personal relationships that could have appeared to influence the work reported in this paper.

Supplementary materials

Supplementary material associated with this article can be found, in the online version, at doi:10.1016/j.actamat.2024.120120.

References

[1] D.O. Northwood, The development and applications of zirconium alloys, Mater. Design 6 (1985) 58–70.

[2] A.T. Motta, A. Couet, R.J. Comstock, Corrosion of zirconium alloys used for nuclear fuel cladding, Annu. Rev. Mater. Res. 45 (2015) 311–343.

[3] D.O. Northwood, U. Kosasih, Hydrides and delayed hydrogen cracking in zirconium and its alloys, Int. Mater. Rev. 28 (1983) 92–121.

[4] V. Macdonald, D.L. Boulch, A.H. de Menibus, J. Besson, Q. Auzoux, J. Crépin, T. L. Jolu, Fracture of Zircaloy-4 fuel cladding tubes with hydride blisters, Proc. Mater. Sci. 3 (2014) 233–238.

[5] Y.J. Jia, W.Z. Han, Effect of external stress on hydride reorientation in zirconium, Acta Mater 235 (2022) 118100.

[6] Y.J. Jia, W.Z. Han, Mechanisms of hydride nucleation, growth, reorientation and embrittlement in zirconium: a review, Materials 16 (2023) 2419.

[7] X.H. Lin, I.J. Beyerlein, W.Z. Han, Annealing cracking in Zr and a Zr-alloy with low hydrogen concentration, J. Mater. Sci. Tech. 182 (2024) 165–175.

[8] J.F.K. Amber, Grain boundary hydride habit in Zircaloy-2, J. Nucl. Mater. 28 (1968) 237–245.

[9] C.E. Ells, Hydride precipitates in zirconium alloys (a review), J. Nucl. Mater. 28 (1968) 129–151.

[10] M.P. Puls, The effects of misfit and external stresses on terminal solid solubility in hydride-forming metals, Acta Metall. 29 (1981) 1961–1968.

[11] K. Une, S. Ishimoto, EBSP measurements of hydrogenated Zircaloy-2 claddings with stress-relieved and recrystallized annealing conditions, J. Nucl. Mater. 357 (2006) 147–155.

[12] N.A.P. Kiran Kumar, J.A. Szpunar, Z. He, Preferential precipitation of hydrides in textured zircaloy-4 sheets, J. Nucl. Mater. 403 (2010) 101–107.

[13] S.Y. Wang, F. Giuliani, T.B. Britton, Microstructure, and formation mechanisms of δ-hydrides in variable grain size Zircaloy-4 studied by electron backscatter diffraction, Acta Mater. 169 (2019) 76–87.

[14] Y.J. Jia, I.J. Beyerlein, W.Z. Han, Precipitation characteristics and distributions of subsurface hydrides in zirconium, Acta Mater. 216 (2021) 117146.

[15] S. Wang, S. Li, R. Li, Y. Wang, N. Xua, F. Xue, G. Bai, Y.D. Wang, Microscopic stress and crystallographic orientation of hydrides precipitated in Zr-1Nb-0.01Cu cladding tube investigated by high-energy X-ray diffraction and EBSD, J. Nucl. Mater. 542 (2020) 152534.

[16] S. Liang, S. Wang, D. An, F. Ma, Y. Jia, X.Z. Wang, S. Li, W. Gong, Y. Wang, Hydride precipitation dependence on α-parent orientation and plastic deformation in zirconium alloys, Acta Mater. 259 (2023) 119292.

[17] W. Qin, J.A. Szpunar, J. Kozinski, Hydride-induced degradation of hoop ductility in textured zirconium-alloy tubes: a theoretical analysis, Acta Mater. 60 (2012) 4845–4855.

[18] K.V. Mani Krishna, A. Sain, I. Samajdar, G.K. Dey, D. Srivastava, S. Neogy, R. Tewari, S. Banerjee, Resistance to hydride formation in zirconium: an emerging possibility, Acta Mater. 54 (2006) 4665–4675.

[19] X.Q. Ma, S.Q. Shi, C.H. Woo, L.Q. Chen, Phase-field simulation of hydride precipitation in bi-crystalline zirconium, Scr. Mater. 47 (2002) 237–241.

[20] G.M. Han, Y.F. Zhao, C.B. Zhou, D.Y. Lin, X.Y. Zhu, J. Zhang, S.Y. Hu, H.F. Song, Phase-field modeling of stacking structure formation and transition of δ-hydride precipitates in zirconium, Acta Mater. 165 (2019) 528–546.

[21] K.B. Colas, A.T. Motta, J.D. Almer, M.R. Daymond, M. Kerr, A.D. Banchik, P. Vizcaino, J.R. Santisteban, In situ study of hydride precipitation kinetics and re-orientation in Zircaloy using synchrotron radiation, Acta Mater. 58 (2010) 6575–6583.

[22] F. Long, S. Hanlon, M.R. Daymond, Transformation behavior of hydrides precipitated with or without stress in Zr-2.5Nb investigated by in-situ S/TEM thermal cycling, J. Nucl. Mater. 559 (2022) 153428.

[23] S.M. Liu, A. Ishii, S.B. Mi, S. Ogata, J. Li, W.Z. Han, Dislocation-mediated hydride precipitation in zirconium, Small 18 (2022) 2105881.

[24] H. Jang, D. Farkas, J.T.M. De Hosson, Determination of grain boundary geometry using TEM, J. Mater. Res. 7 (1992) 1707–1717.

[25] W. Qin, N.A.P. Kiran Kumar, J.A. Szpunar, J. Kozinski, Intergranular δ-hydride nucleation and orientation in zirconium alloys, Acta Mater 59 (2011) 7010–7021.

[26] W.C. Johnson, C.L. White, P.E. Marth, P.K. Ruf, S.M. Tuominen, K.D. Wade, K. C. Russell, H.I. Aaronson, Influence of crystallography on aspects of solid-solid nucleation theory, Metall. Trans. A 6 (1975) 911–919.

[27] M.P. Puls, Hydrogen-induced delayed cracking: 2. Effect of stress on nucleation, growth and coarsening of zirconium hydride precipitates, Atomic Energy of Canada Limited Report, AECL-8381 Atomic Energy of Canada, Mississauga, Ontario (1984).

[28] M. Kolesnik, T. Aliev, V. Likhanskii, Modeling of size, aspect ratio, and orientation of flattened precipitates in the context of Zr-H system under external stress, Comp. Mater. Sci. 189 (2021) 110260.

[29] H.I. Aaronson, M. Enomoto, J.K. Lee, Mechanisms of Diffusion Phase Transformations in Metals and Alloys, CRC Press, 2010.

[30] J.E. Bailey, Electron microscope observations on the precipitation of zirconium hydride in zirconium, Acta Metall. 11 (1963) 267–280.

[31] M.A. Tschopp, D.L. McDowell, Structures and energies of Σ3 asymmetric tilt grain boundaries in copper and aluminium, Philos. Mag. 87 (2007) 3147–3173.

[32] A.J. Plowman, C.P. Race, A first principles study of zirconium grain boundaries, J. Nucl. Mater. 568 (2022) 153853.

[33] Z. Xue, X. Zhang, J. Qin, M. Ma, R. Liu, Exploring the effects of solute segregation on the strength of Zr {1011} grain boundary: a first-principles study, J. Alloy. Comp. 812 (2020) 152153.

[34] E. Torres, Atomistic study of the structure and deformation behavior of symmetric tilt grain boundaries in α-zirconium, Comp. Mater. Sci. 197 (2021) 110600.

[35] I. Ghamarian, P. Samimi, G.S. Rohrer, P.C. Collins, Determination of the five-parameter grain boundary character distribution of nanocrystalline alpha-zirconium thin films using transmission electron microscopy, Acta Mater. 130 (2017) 164–176.

[36] S.M. Liu, S.H. Zhang, S. Ogata, H.L. Yang, S. Kano, H. Abe, W.Z. Han, Direct observation of vacancy-cluster-mediated hydride nucleation and the anomalous precipitation memory effect in zirconium, Small (2023) 2300319.

[37] C. Varvenne, O. Mackain, L. Proville, E. Clouet, Hydrogen and vacancy clustering in zirconium, Acta Mater. 102 (2016) 56–69.

[38] Y. Zhao, M.N. Polyakov, M. Mecklenburg, M.E. Kassner, A.M. Hodge, The role of grain boundary plane orientation in the β phase precipitation of an Al–Mg alloy, Scripta Mater. 89 (2014) 49–52.

[39] W.T. Read, W. Shockley, Dislocation models of crystal grain boundaries, Phys. Rev. 78 (1950) 275–289.

[40] A. Tondro, H. Abdolvand, Quantifying hydrogen concentration in the vicinity of zirconium hydrides and deformation twins, J. Mech. Phys. Solids 148 (2021) 104287.

[41] I.A. Khan, A.C.F. Cocks, J. Chattopadhyay, A study of hydride precipitation in zirconium, Mech. Mater. 155 (2021) 103773.

[42] D.P.A. Singh, Effect of symmetrical and asymmetrical tilt grain boundaries on radiation-induced defects in zirconium, J. Phys. D. Appl. Phys. 51 (2018) 265301.

[43] A. Arjhangmehr, S.A.H. Feghhi, Irradiation deformation near different atomic grain boundaries in α-Zr: an investigation of thermodynamics and kinetics of point defects, Sci. Rep. 6 (2016) 23333.

[44] F. Hatami, S.A.H. Feghhi, A. Arjhangmehr, A. Esfandiarpour, Interaction of primary cascades with different atomic grain boundaries in a-Zr: an atomic scale study, J. Nucl. Mater. 480 (2016) 362–373.

[45] J. von Pezold, L. Lymperakis, J. Neugebeauer, Hydrogen-enhanced local plasticity at dilute bulk H concentrations: the role of H-H interactions and the formation of local hydrides, Acta Mater. 59 (2011) 2969–2980.